

Arresting doubly excited electronic state mediating lightning speed ring-opening reaction of 1,3-cyclohexadiene

Shutaro Karashima,¹ Ryuta Uenishi,¹ Takuya Horio,^{1†} Manabu Kanno,² Alexander Humeniuk,³ Roland Mitrić,³ Tetsuro Ohta,¹ Junichi Nishitani,¹ and Toshinori Suzuki^{1*}

¹Department of Chemistry, Graduate School of Science, Kyoto University, Kyoto 606-8502, Japan

²Department of Chemistry, Graduate School of Science, Tohoku University, Sendai 980-8578, Japan

³Universität Würzburg, Institut für Physikalische und Theoretische Chemie, Emil-Fischer-Str. 42, 97074 Würzburg, Germany

Supplementary Information

S1. Experimental Apparatus

Our extreme UV (XUV) time-resolved photoelectron spectroscopy (TRPES) experiment was performed using a single harmonic XUV light source¹ and a filamentation four-wave mixing deep UV (DUV) light source.² While we have employed these light sources separately in our previous studies, the present study demonstrates their first combined use. A schematic diagram of our optical setup and photoelectron spectrometer is shown in Fig. S1. The 2.4 and 1.8 mJ beams were separated from the output of a one-box Ti:sapphire regenerative amplifier (Coherent Astrella, 35 fs, 800 nm, 1 kHz, 6 mJ), and the pump (267 nm, 4.6 eV) and probe (57 nm, 21.7 eV) pulses were generated. A commercial beam pointing stabilizer was used to lock the pointing of the 800 nm beam.

The probe pulses were generated using a high-harmonic generation (HHG) process in a rare gas.³⁻⁵ The fundamental beam was frequency-doubled in a β -barium borate (BBO; $\theta = 29^\circ$, 0.3-mm thickness) crystal to obtain the second harmonic (2ω) beam (0.29 mJ), which was then focused using a quartz convex lens ($f = 500$ mm) into a Teflon tube in the HHG chamber through a laser-drilled pinhole. The Teflon tube (6.35 mm inner diameter) was filled with Kr gas at 43 Torr, and the gas leaking through the laser-drilled pinholes was evacuated with a turbo molecular pump (480 L/sec) backed up by a dry pump (600 L/min). A copper plate with an aperture ($\varnothing 2$ mm) was installed at the end of the HHG chamber to enable differential pumping. The vacuum pressure in the HHG chamber was kept at $< 3.8 \times 10^{-4}$ Torr during operation. The high harmonics were then introduced into a time-preserving monochromator,⁶ which consisted of toroidal mirrors and a grating (groove density 150 gr/mm; blaze angle 6.2°) to select the 14th harmonic (14ω : 57 nm, 21.7 eV). The pressure in the optics chamber was maintained at $< 1.0 \times 10^{-5}$ Torr during the experiment using four turbo molecular pumps (76, 210, 210 and 400 L/sec) backed by dry pumps (500 and 600 L/min).

For the filamentation four-wave mixing light source, the fundamental beam (ω , 0.5 mJ) and the second harmonic beam (2ω , 0.3 mJ) generated in a β -BBO ($\theta = 29^\circ$, 0.3-mm thickness) were focused using concave mirrors ($r = -2000$ mm) into an Ar gas cell (30 Torr) through a Brewster-angled CaF_2 window (1-mm thickness). When the ω and 2ω pulses were overlapped temporally and spatially, DUV and vacuum UV (VUV) pulses were generated by a cascaded four-wave mixing process. We employed a flat Al disk with a laser-drilled pinhole (1.5-mm thickness) and a narrow channel ($\varnothing 2.5$ mm, 18-mm thickness) to reduce gas

conductance between the gas cell and the optics chamber to facilitate differential pumping. The Ar gas leaking through the pinhole was evacuated using a dry pump (250 L/min) in the differential pumping section. The output pulses were reflected with multi-layer mirrors designed for 3ω and focused by concave mirrors ($r=-2500$ and -3000 mm) into the ionization chamber. The optical path length of the 3ω pulses was controlled using a translation stage with 5-nm resolution installed in the optics chamber. The pulse width and energy of the pump beam were sub-30 fs and 800 nJ/pulse, respectively. Material dispersion was avoided by having all optical path under vacuum and no transmitting optical components. The cross-correlation time between the pump and probe pulses was measured to be 48 fs by non-resonant ionization of Xe, as shown in Fig. S2.

The vapor of 1,3-cyclohexadiene (CHD) seeded in a He carrier gas (about 4%) was injected into the photoelectron spectrometer through a pinhole ($\varnothing 0.1$ mm) at a stagnation pressure of 0.06 MPa at room temperature. The photoionization chamber was evacuated with a turbo molecular pump (1380 L/s) to maintain its pressure at 4.0×10^{-5} Torr. The photoelectron kinetic energy (PKE) distribution was measured using a magnetic bottle time-of-flight electron spectrometer,⁷ which used a combination of a strong magnetic field produced by a SmCo magnet (300 mT) and a weak magnetic field produced by a solenoid coil (300 turns/m, 3 A, 1 mT) to enable collection of more than 50% of the photoelectrons. A graphite coated entrance skimmer ($\varnothing 1$ mm) located 3 mm from the ionization point facilitated differential pumping of the electron spectrometer, which was evacuated using a turbo molecular pump (2000 L/s) to maintain a pressure of 1.0×10^{-7} Torr during the experiment. The gas nozzle and magnet were also coated with graphite and electrically grounded. A permalloy inner layer was installed in the entire apparatus, including the photoionization chamber and the magnetic bottle electron spectrometer, to shield them from the terrestrial magnetic field. The electron flight length was 1,300 mm, and a microchannel plate detector (MCP, $\varnothing 42$ mm) at the end of the flight tube detected electrons. The electric signal from the MCP was preamplified and measured using an A/D converter. A retardation voltage of -6.0 V was applied to the flight tube in order to reject the low-energy electrons produced by one-color two-photon ionization by the pump pulses; thus, the detectable PKE range was restricted to greater than 6 eV. Energy calibration of the spectrometer was performed using the $^2P_{3/2}$ and $^2P_{1/2}$ peaks in the photoelectron spectrum of Xe. The energy resolution was estimated to be 120 meV from the band width shown in Fig. S3. Both the pump and probe laser pulses were linearly polarized parallel to the electron flight axis.

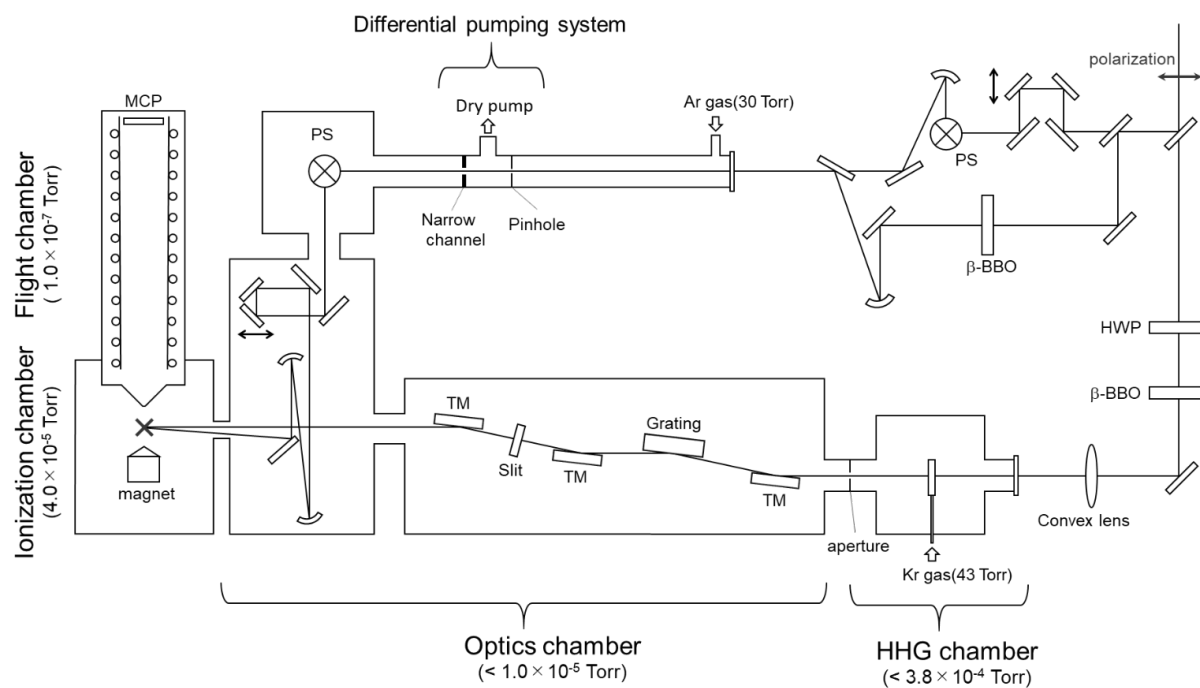


Figure S1 Schematic diagram of optical setup and vacuum chambers. The red cross indicates the ionization point. (HWP: half wave plate, PS: periscope, TM: toroidal mirror, MCP: microchannel plate)

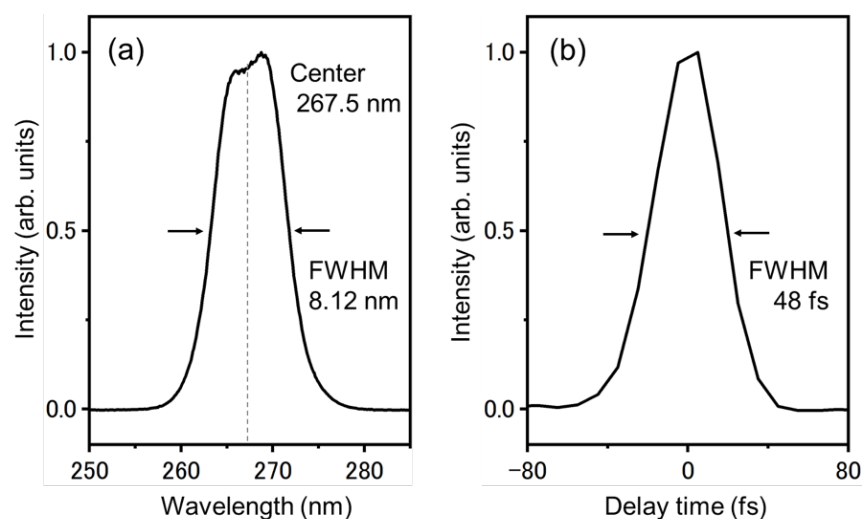


Figure S2 Characteristics of DUV and XUV pulses. (a) Spectrum of DUV pump pulses measured using a UV spectrometer, and (b) time profile of non-resonant photoionization signal of xenon with the DUV pump and XUV probe pulses.

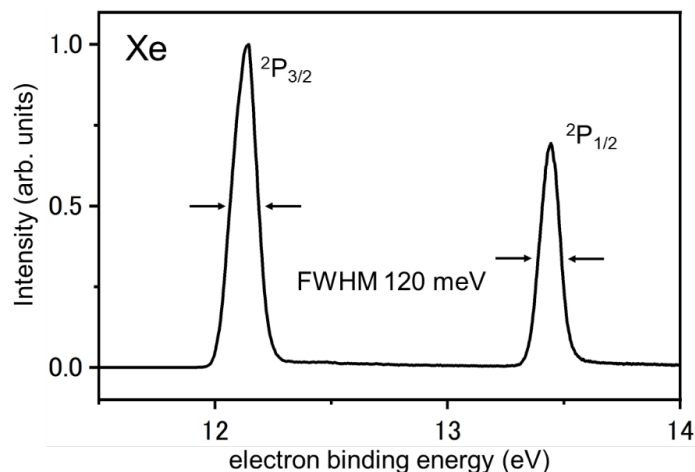


Figure S3 Energy resolution of apparatus. Photoelectron spectrum of xenon gas measured using magnetic bottle time-of-flight electron spectrometer with XUV pulses (21.7 eV).

S2. Global fitting of photoelectron spectra and least-squares fitting of photoelectron intensity time profiles

We performed a global fitting analysis of the time-resolved photoelectron spectra in the eBE region between 3 and 7.7 eV. We used seven Gaussian and one exponential function as the basis set. The fitting function is expressed as

$$f(E, t) = \sum_{i=1}^7 c_i(t) \exp\left(-\frac{(E-Ec_i)^2}{2w_i^2}\right) + c_8(t)\exp(kE) \quad (\text{S1})$$

where E is eBE, t is the delay time between the pump and probe pulses, c_i is an expansion coefficient, Ec_i and w_i are the center and width of the Gaussian, respectively, and k is a constant. The first term in (S1) expresses the main photoelectron bands, which rapidly change with time, and the second term describes a small foot of the strong photoelectron band centered at 8.4 eV. The actual value of k was determined separately by analysis of the spectral intensity between delay times of 250 and 300 fs, and this value was fixed in the global fitting. The contribution of this component was very small. The results are shown in Figs. S4 and S5 and Table S1. Three bands were confirmed as ionization from the 1^1B state, and one band from the 2^1A state.

We also tried to find a kinetic model that describes the population in each electronic state, and we found that the model shown in Fig. S6 provides good agreement with the experimental data. In this kinetic model, the population in each state is expressed analytically as follows,

$$[1^1\text{B}] = \begin{cases} 0 & (t < 0) \\ 1 & (0 \leq t \leq t_d) \\ x \cdot \exp(-k_1 t') & (t_d < t) \end{cases} \quad (\text{S2})$$

$$[2^1\text{A}] = \begin{cases} 0 & (t < t_d) \\ \exp(-k_2 t') + \frac{x}{K_{21}} \{k_1 \exp(-k_1 t') - k_2 \exp(-k_2 t')\} & (t_d \leq t) \end{cases} \quad (\text{S3})$$

$$[1^1\text{A}]_{\text{nascent}} = \begin{cases} 0 & (t < t_d) \\ \frac{x k_2 k_1}{K_{31} K_{21}} \exp(-k_1 t') + \frac{k_2 (K_{21} - x k_2)}{K_{32} K_{21}} \exp(-k_2 t') - \frac{k_2 (K_{31} - x k_3)}{K_{32} K_{31}} \exp(-k_3 t') & (t_d \leq t) \end{cases} \quad (\text{S4})$$

$$[1^1\text{A}]_{\text{relaxed}} = \begin{cases} 0 & (t < t_d) \\ \frac{x k_2 k_1}{K_{31} K_{21}} \{1 - \exp(-k_1 t')\} + \frac{k_2 (K_{21} - x k_2)}{K_{32} K_{21}} \{1 - \exp(-k_2 t')\} - \frac{k_2 (K_{31} - x k_3)}{K_{32} K_{31}} \{1 - \exp(-k_3 t')\} & (t_d \leq t) \end{cases} \quad (\text{S5})$$

where k_i is the reaction rate constant, t_d is the induction time prior to population decay, x is the fraction of the population remaining in the 1^1B state while passing through the conical intersection (CoIn) region, $t' = t - t_d$, and $K_{ij} = k_i - k_j$. The experimental results indicate that there is a finite induction (or latency) time for the population decay from the excited state(s), and our model assumes, for simplicity, that the population decay starts immediately after the system enters the 2^1A electronic state. Consequently, t_d becomes the arrival time of the wave packet to the 1^1B - 2^1A CoIn. However, in reality, the wave packet is expected to propagate on the 2^1A surface to arrive at the 2^1A - 1^1A CoIn region and start decaying to the 1^1A state. Therefore, it is likely that there is a time lag between the arrival time of the wave packet at the former and the latter CoIn. Thus, t_d provides the upper bound for the arrival time of the wave packet at the first CoIn. However, as shown later, the experimentally extracted value of t_d agrees well with the theoretically calculated value. Our experimental data also show that the signal intensities for the first and second bands of the reaction products, in the regions of 7.5-8.0 and 9.0-10.0 eV, respectively, slightly diminish with time, either due to a small upshift of these bands or band narrowing. In order to express this subtle spectral evolution of the reaction products and evaluate the reaction product population accurately, we defined two subsets for the 1^1A state of the products, namely nascent and slightly relaxed vibrational states, and assumed a phenomenological dephasing rate constant k_3 to express the time evolution from the former to the latter. As listed in Table S2, the time scale for this relaxation is 18 ps. Since the 1,3,5-hexatriene (HT) product undergoes significant structural changes among cZc , tZc , tZt isomers on a sub-picosecond time scale, the nature of the vibrational relaxation expressed by k_3 is not readily clear. It is a phenomenological time constant.

Thus, the total photoelectron signal intensity is expressed by

$$I(t) = \left(C_1[1^1\text{B}] + C_2[2^1\text{A}] + C_3[1^1\text{A}]_{nascent} + C_4[1^1\text{A}]_{relax} \right) \otimes G(t) \quad (\text{S6})$$

where C_i is the expansion coefficient and $G(t)$ is a Gaussian-shaped cross-correlation function for the laser pulses. We also added the following function to phenomenologically express the vibrational quantum beats observed in the time profile of the 1^1A signal,

$$I'(t) = I(t) + \left\{ C_5 \cos\left(\frac{2\pi t''}{T_1}\right) + C_6 \cos\left(\frac{2\pi t''}{T_2}\right) \right\} \left\{ \exp(-k_4 t'') \otimes G(t) \right\} \quad (\text{S7})$$

where $t'' = t - t_{onset}$ (elapsed time from the time origin for oscillation t_{onset}), and T_i is the period of oscillation. The results of least-squares fitting are shown in Fig. S7 and Table S2.

Table S1 Parameters determined by global fitting analysis.

i	Ec_i	w_i	assignment
1	3.91	0.200	} $1^2\text{A} \leftarrow 1^1\text{B}$ (including the spectral shift)
2	4.38	0.342	
3	5.06	0.362	
4	6.10	0.310	$1^2\text{A} \leftarrow 2^1\text{A}$
5	6.26	0.207	$1^2\text{B} \leftarrow 1^1\text{B}$
6	6.62	0.198	Not assigned yet
7	7.15	0.414	2^2B or $3^2\text{B} \leftarrow 1^1\text{B}$

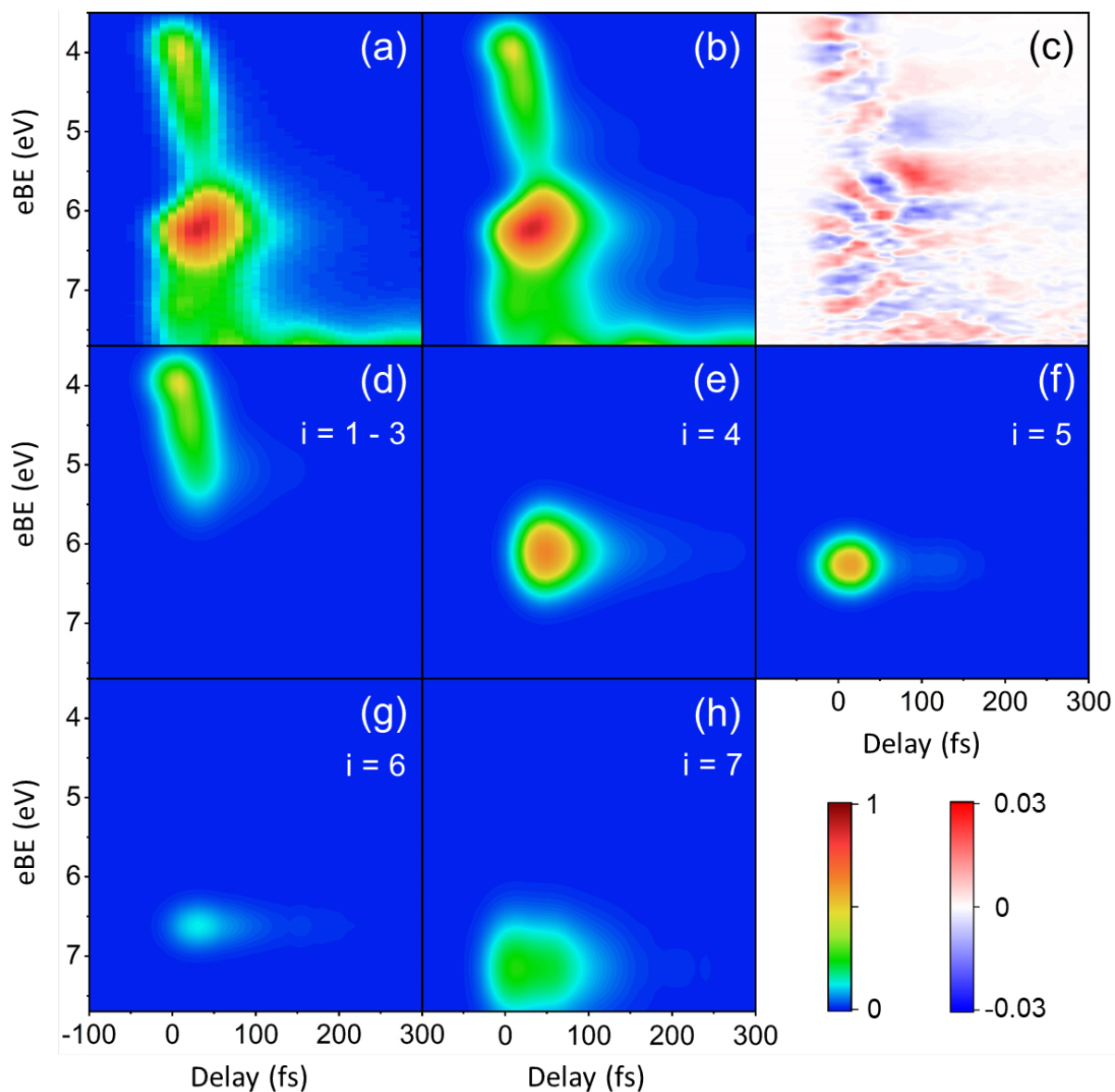


Figure S4 Experimental photoelectron spectra and simulated spectra. (a) Experimental photoelectron spectra. (b) Simulated spectra by least-squares fitting, which is the sum of (d) – (h). (c) The residual, which is the difference between (a) and (b). (d)-(h) spectral components determined by least-squares fitting.

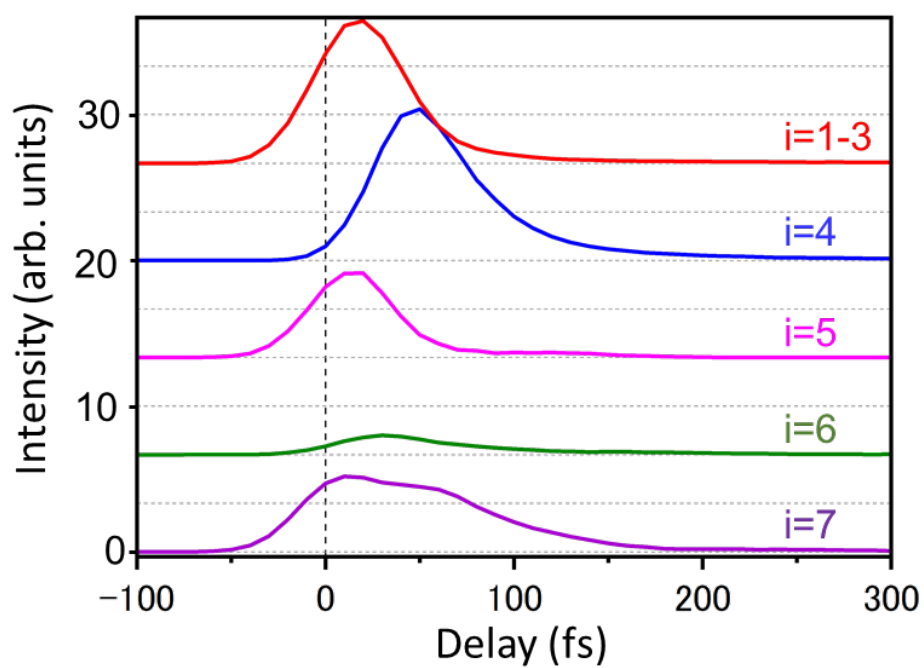


Figure S5 Intensity time profiles spectrally integrated over eBE.

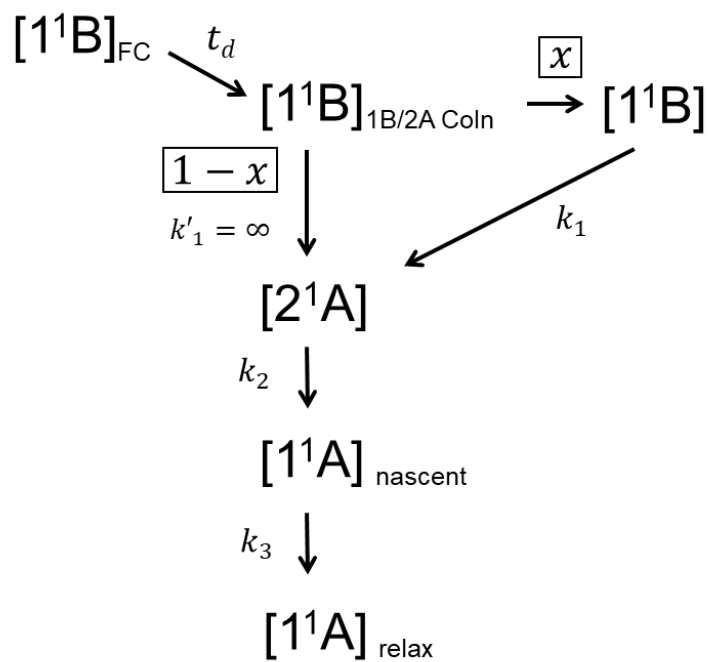


Figure S6 Kinetic model. (FC: Franck-Condon, CoIn: conical intersection)

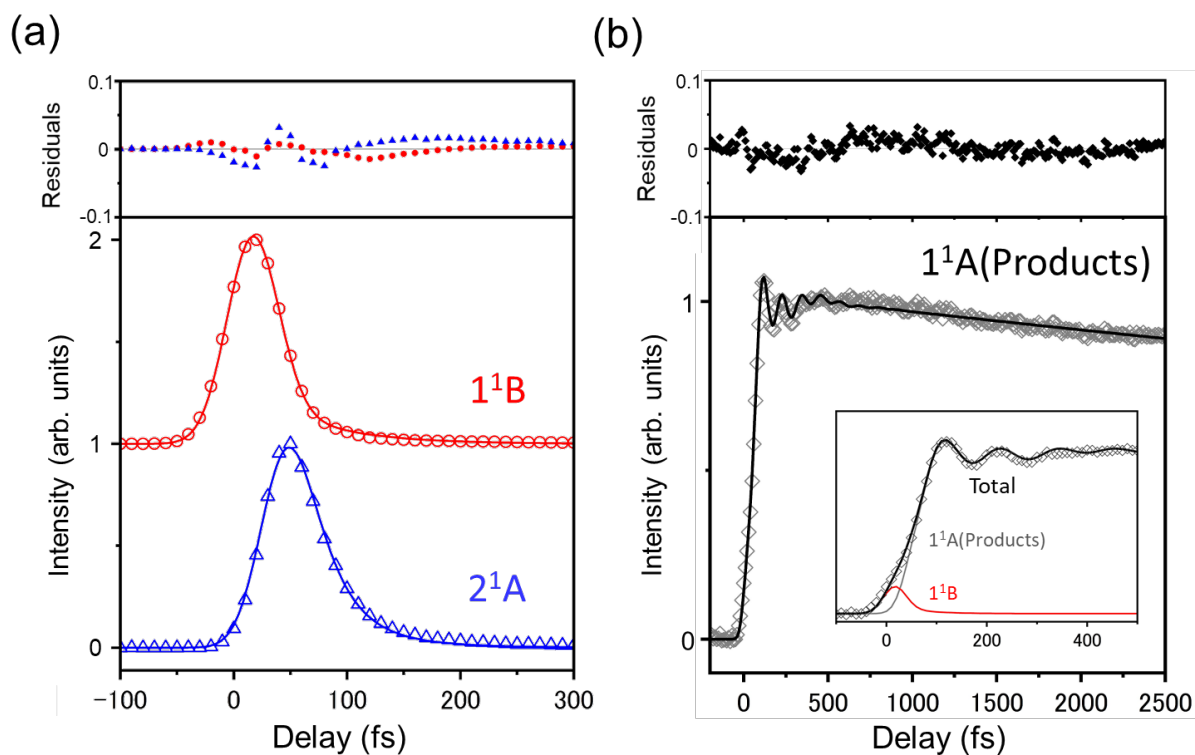


Figure S7 Population in the electronic states of (a) 1^1B , 2^1A and (b) 1^1A . Open symbols in the main panels show the intensity extracted from the experimental data and the solid line is the best-fit profile. Filled symbols in the upper panels show the residuals. The intensity profiles for 1^1B and 2^1A in (a) were obtained from the kinetics components of $i=1-3$ and $i=4$, respectively. The intensity of 1^1A in (b) is the time profile at an eBE of 10 eV. The inset in (b) shows an expanded view around the time origin along with the population in the 1^1B (red) and 1^1A (gray) states. The oscillations seen in (b) are vibrational quantum beats in then reaction products.

Table S2 Best-fit parameters determined by least-squares fitting of time profiles.

Parameters	Values
$\tau_1 = 1/k_1$	57 fs
$\tau_2 = 1/k_2$	24 fs
$\tau_3 = 1/k_3$	18 ps
$\tau_4 = 1/k_4$	162 fs
T_1	115 fs (290 cm^{-1})
T_2	424 fs (79 cm^{-1})
t_{onset}	57 fs
t_d	32 fs
x	0.12

S3. Analysis of vibrational quantum beats in photoelectron signal intensity

The time profiles of the photoelectron signal intensity measured at eBE values of 8.0, 8.3 and 10.0 eV are shown in Fig. S8. The bottom profile is identical to that shown in Fig. S7(b). Oscillatory features due to vibrational quantum beats are clearly seen at 8.0 and 10.0 eV. In the main text, we describe the least-squares fitting of these profiles using Eq. (S7): the best-fit parameters are listed in Table S3.

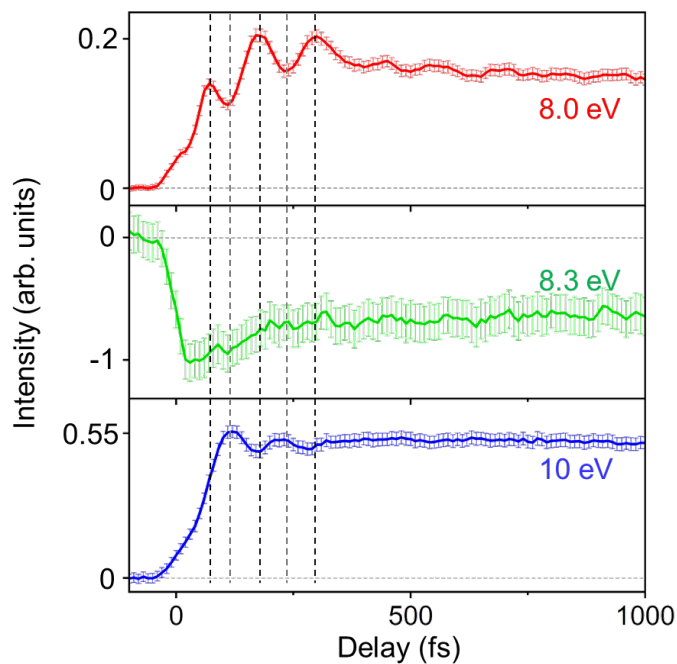


Figure S8 Time profiles measured at eBE values of 8.0, 8.3 and 10.0 eV. The bars are the standard deviation.

Table S3 Best-fit parameters determined by least-squares fitting of reaction product signals.

Parameters	First band (8 eV)	Second band (10 eV)
$\tau_1 = 1/k_1$	57 fs (fixed)	
$\tau_2 = 1/k_2$	24 fs (fixed)	
$\tau_3 = 1/k_3$	780 fs	18 ps
$\tau_4 = 1/k_4$	209 fs	162 fs
T_4	127 fs (263 cm ⁻¹)	115 fs (290 cm ⁻¹)
T_5	528 fs (63 cm ⁻¹)	424 fs (79 cm ⁻¹)
t_{onset}	53 fs	57 fs
t_d	32 fs (fixed)	
x	0.12 (fixed)	

S4. Computational details

The effective potential energy curves for the ring-opening reaction of CHD were computed using the Roos atomic natural orbital (ANO) basis set⁸ contracted to 4s3p2d functions for carbon and 2s1p functions for hydrogen using the *ab initio* quantum chemistry software MOLPRO.^{9,10} For neutral CHD, static electron correlation was treated at the complete-active-space self-consistent field (CASSCF) level of theory^{11,12} with an active space composed of six electrons distributed among six orbitals, namely, two π and two π^* orbitals in addition to one σ and one σ^* orbitals initially localized at the breaking C₅-C₆ bond. The CASSCF orbitals were averaged over the states of interest (1^1A , 1^1B and 2^1A) with equal weights. Dynamic electron correlation was then taken into account at the level of the extended multi-state CAS second-order perturbation theory (XMS-CASPT2)^{13,14} with a level shift of 0.3 Hartree adopted to avoid intruder state problems.¹⁵ The geometry of CHD was optimized in the 1^1A and 2^1A states under C_2 symmetry constraints. Along the path linearly connecting the two optimized geometries, the three neutral states were evaluated in the multi-state multi-reference (MS-MR) scheme of XMS-CASPT2. A number of cationic states accessible from the neutral states by a 21.7-eV photon were also obtained in the single-state single-reference (SS-SR) scheme of XMS-CASPT2 with a larger active space of 31 electrons in 17 (fourteen σ , two π and one π^*) orbitals. Figure S9 shows the calculated potential energy curves for 1^1A , 1^1B , 2^1A , 1^2A , 1^2B , 2^2A , 2^2B , 3^2A and 3^2B for CHD, and Table S4 summarizes their energies at the Franck-Condon state and the 2^1A equilibrium geometry.

The ionization energies for three isomers of HT were computed in a similar manner. The geometry optimization of neutral HT in the 1^1A state was carried out at the CASPT2 level with an active space consisting of six electrons in six (three π and three π^*) orbitals. The resultant equilibrium geometries of the *cZc*, *cZt* and *tZt* isomers were of C_2 , C_1 and C_{2v} symmetry, respectively. Cationic states reachable from the 1^1A state for each isomer were evaluated in SS-SR scheme of XMS-CASPT2 with an active space of 31 electrons in 17 (thirteen σ , three π and one π^*) orbitals. The calculated ionization energies (vertical eBEs) for the three isomers are summarized in Table S5 along with those for CHD in the 1^1A state.

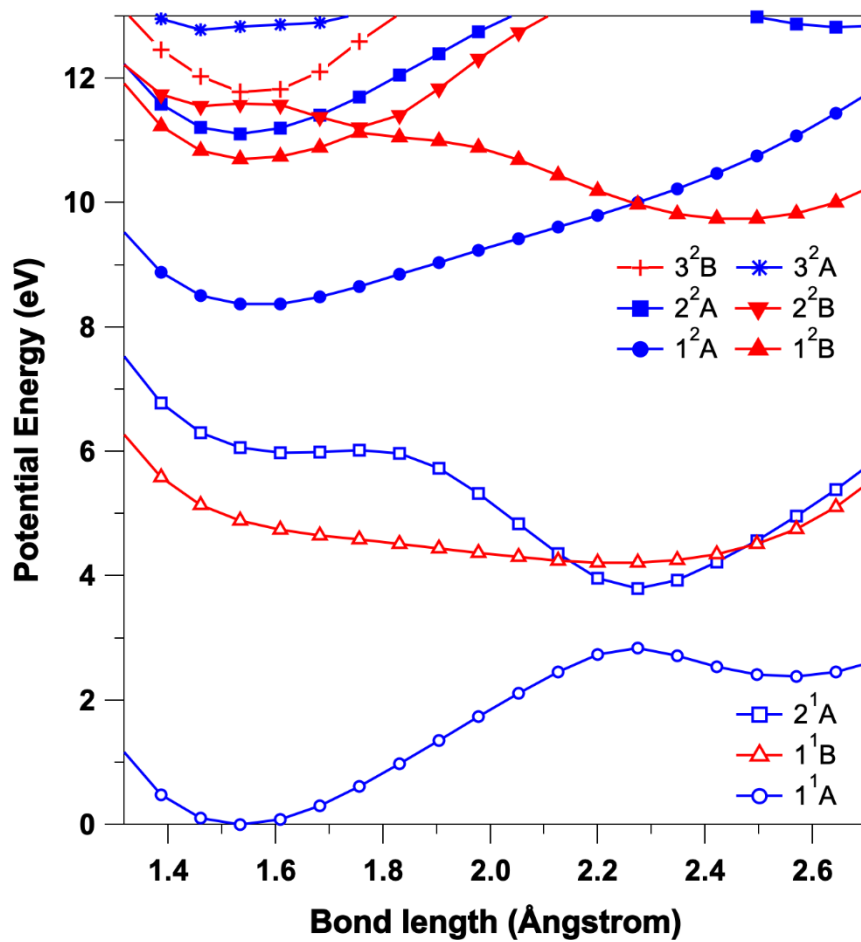


Figure S9 Calculated potential energy curves for 1^1A , 1^1B , 2^1A , 1^2A , 1^2B , 2^2A , 2^2B , 3^2A and 3^2B for CHD along the ring opening coordinate (see text).

Table S4 Calculated XMS-CASPT2 energies (eV) for 1¹A, 1¹B, 2¹A, 1²A, 1²B, 2²A, 2²B and 3²B states of CHD along with experimental values in literature.

State	Franck-Condon		2 ¹ A equilibrium		
	Leading Configuration	Calc.	Exp.	Leading Configuration(s)	Calc.
3 ² B	$\cdots(9b)^2(11a)^2(10b)^2(\mathbf{12a})^0(\mathbf{11b})^1$	11.78	11.8 ^a	$\cdots(10a)^2(10b)^2(\mathbf{11a})^1(\mathbf{11b})^1(\mathbf{12a})^1$	13.72
2 ² B	$\cdots(\mathbf{9b})^1(11a)^2(10b)^2(12a)^2(11b)^0$	11.60	11.8 ^b	$\cdots(10a)^2(\mathbf{10b})^1(11a)^2(11b)^2(12a)^0$ $\cdots(10a)^2(\mathbf{10b})^1(11a)^2(11b)^0(12a)^2$	13.09
2 ² A	$\cdots(9b)^2(\mathbf{11a})^1(10b)^2(12a)^2(11b)^0$	11.11	11.3 ^b	$\cdots(10a)^2(10b)^2(\mathbf{11a})^1(11b)^2(12a)^0$ $\cdots(10a)^2(10b)^2(\mathbf{11a})^1(11b)^0(12a)^2$	13.16
1 ² B	$\cdots(9b)^2(11a)^2(\mathbf{10b})^1(12a)^2(11b)^0$	10.70	10.7 ^b	$\cdots(10a)^2(10b)^2(11a)^2(\mathbf{11b})^1(12a)^0$	9.98
1 ² A	$\cdots(9b)^2(11a)^2(10b)^2(\mathbf{12a})^1(11b)^0$	8.37	8.25 ^b	$\cdots(10a)^2(10b)^2(11a)^2(11b)^0(\mathbf{12a})^1$	10.00
2 ¹ A	$\cdots(9b)^2(11a)^2(\mathbf{10b})^1(12a)^2(\mathbf{11b})^1$	6.06 ^c	–	$\cdots(10a)^2(10b)^2(11a)^2(11b)^2(12a)^0$ $\cdots(10a)^2(10b)^2(11a)^2(11b)^0(12a)^2$	3.80
	3s Rydberg state ^d				
1 ¹ B	$\cdots(9b)^2(11a)^2(10b)^2(\mathbf{12a})^1(\mathbf{11b})^1$	4.88	4.94 ^f	$\cdots(10a)^2(10b)^2(11a)^2(\mathbf{11b})^1(\mathbf{12a})^1$	4.21
1 ¹ A	$\cdots(9b)^2(11a)^2(10b)^2(12a)^2(11b)^0$	0	0	$\cdots(10a)^2(10b)^2(11a)^2(11b)^2(12a)^0$ $\cdots(10a)^2(10b)^2(11a)^2(11b)^0(12a)^2$	2.83

^a This work. The absorption spectrum of CHD cation in a freon matrix¹⁶ suggests 11.5 eV. The 3²B and 2²B are almost degenerate, and their energetic orders are difficult to determine.

^b He I PES.¹⁷

^c Classified as 4¹A at the F.C. geometry.

^d The leading configuration is $\cdots(9b)^2(11a)^2(10b)^2(12a)^1(11b)^0(13a)^1$. The state energy was calculated in the MS-MR scheme of XMS-CASPT2 with an active space of four electrons in eight orbitals, namely, two π and two π^* orbitals in addition to 3s, 3p_x, 3p_y and 3p_z Rydberg orbitals. 13a is of 3s Rydberg character.

^e Resonant enhanced multiphoton ionization.¹⁸

^f Optical and electron energy loss spectroscopies.¹⁹

Table S5 Ionization energies (vertical eBEs) in units of eV calculated for three HT isomers of *cZc*, *cZt* and *tZt*, along with those for CHD. Only the cationic states accessible from their electronic ground states within the frozen orbital approximation are shown.

<i>cZc</i> (C_2)	HT		CHD (C_2)
	<i>cZt</i> (C_1)	<i>tZt</i> (C_{2v})	
15.92 (9^2B)	–	–	16.17 (8^2A)
15.60 (9^2A)	15.25 (16^2A)	15.55 (5^2A_1)	15.72 (7^2B)
14.82 (7^2B)	14.48 (13^2A)	14.71 (4^2A_1)	14.82 (6^2B)
13.91 (5^2A)	14.10 (10^2A)	14.04 (3^2B_2)	13.90 (5^2A)
13.64 (4^2A)	13.26 (8^2A)	13.38 (2^2B_2)	13.79 (4^2B)
13.01 (4^2B)	13.01 (7^2A)	12.84 (2^2A_1)	13.28 (4^2A)
12.26 (3^2A)	12.36 (6^2A)	12.41 (1^2A_1)	12.84 (3^2A)
11.74 (3^2B)	11.62 (4^2A)	11.77 (2^2B_1)	11.60 (2^2B)
10.68 (2^2B)	10.98 (3^2A)	11.54 (1^2B_2)	11.11 (2^2A)
10.05 (1^2A)	9.95 (2^2A)	10.23 (1^2A_2)	10.70 (1^2B)
8.31 (1^2B)	8.24 (1^2A)	8.37 (1^2B_1)	8.37 (1^2A)
0 (1^1A)	0 (1^1A)	0 (1^1A_1)	0 (1^1A)

S5. TRPEI Experiment with 267 nm pump and 197/157 nm probe pulses

In addition to the XUV-TRPES experiments described in the main text, we performed time-resolved photoelectron imaging (TRPEI) with 267 nm (4.7 eV) pump and 197 or 157 nm probe pulses. Since the information obtained using TRPEI is similar to that obtained using XUV-TRPES, we did not discuss these results in the main text, but TRPEI with a higher time resolution (30 fs) confirmed the XUV-TRPES data. The details of the TRPEI instrument have been reported elsewhere.²⁰ Briefly, a supersonic molecular beam of CHD (~5 %) seeded in helium was generated using an Even-Lavie pulsed solenoid valve,²¹ and jet-cooled CHD molecules were excited with 4.7-eV DUV photons that are resonant with the 1^1B state. The subsequent electronic dynamics were probed by single photoionization using time-delayed probe pulses with photon energies of 6.3-eV or 7.8-eV. The energies of the pump and probe pulses were about 50 nJ/pulse and the cross-correlation times for the 4.7/6.3-eV and 4.7/7.8-eV experiments were measured to be 31.5 and 30.9 fs, respectively. These values were obtained

using (1 + 1') non-resonant multiphoton ionization of ethanol and Xe gases, respectively. Photoelectrons were accelerated towards a two-dimensional (2D) position-sensitive detector (microchannel plate + phosphor screen), and a 2D projection of the 3D velocity distribution of the photoelectrons was recorded. In the 4.7/6.3-eV experiment, the images were measured with an approximately 8-fs step from -66.7 to 117.5 fs. Each image at a given delay time was integrated for 13 s, and the measurement was repeated 21 times. In the 4.7/7.8-eV experiment, the measurements were performed with an approximately 8-fs step from -61.7 to 218.5 fs. The integration time for each image at a given delay time was also 13 s for the 4.7/7.8-eV setup, and the measurement was repeated 60 times. pBASEX²² was used to calculate the slice image through the symmetry axis given by the laser polarization and obtain time-dependent photoelectron kinetic-energy distributions (PKEDs).

Figure S10 shows (a) a 2D time-energy map of PKED obtained using the 6.3-eV probe pulses and (b) a map obtained using the 7.8-eV probe pulses. One-color background signals have already been subtracted. An intense sharp peak appearing at an eBE of 3.8 eV in Fig. S10(a) in the negative delay time region is the photoionization signal from the Rydberg state(s) created by the probe-pump pulse sequence; its PKE value is consistent with any of the term values, 6.03, 6.04 and 6.05 eV, respectively, for the $3p_x$, $3p_y$, and $3p_z$ Rydberg states with the ion core of CHD (1^2A).¹⁸ Very recently, Ruddock et al. performed a time-resolved X-ray scattering experiment on CHD with 200 nm pump pulses, and they reported the upper states to be $3p_x$ and $3p_y$.²³ Least-squares fitting of our signal indicated a lifetime of 98 ± 2 fs, which is much shorter than the value of 208 ± 11 fs reported by Ruddock et al.²³ While the S/N ratio in Fig. S10(b) is not as good as that for the XUV data presented in the main text, the results are consistent with each other.

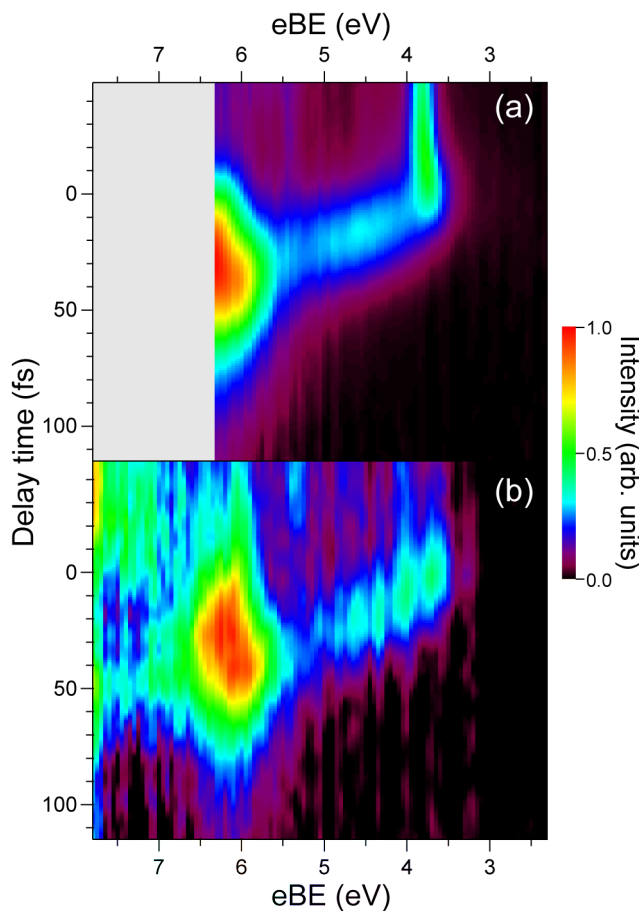


Figure S10 Two-dimensional maps of photoelectron spectra obtained by (a) 4.7/6.3-eV and (b) 4.7/7.8-eV experiments. The horizontal axis is the eBE given by the difference between the probe photon energy (6.3 or 7.8 eV) and the measured electron kinetic energy eKE. Both of these 2D maps were interpolated using a cubic spline such that the intervals between the delay times are 1 fs.

Figure S11 shows a photoelectron time profile obtained for 4.7/7.8-eV TRPEI; the photoelectron intensities were integrated over the eBE region of 2.8-6.8 eV in Fig. 10(b). As seen in Fig. S11, a sub-100 fs decay of the excited-state population is evident. We also performed least-squares fitting of the observed time profile using the kinetic model described in section S2. Owing to the limited S/N ratio in Fig. S11, the x value was not obtainable in this fitting. Nevertheless, the least-squares fitting provided $t_d = 30 \pm 4$ fs and $\tau_2 = 21 \pm 2$ fs, which are in excellent agreement with the values of 32 and 24 fs, respectively, for t_d and τ_2 determined by the XUV probe experiment.

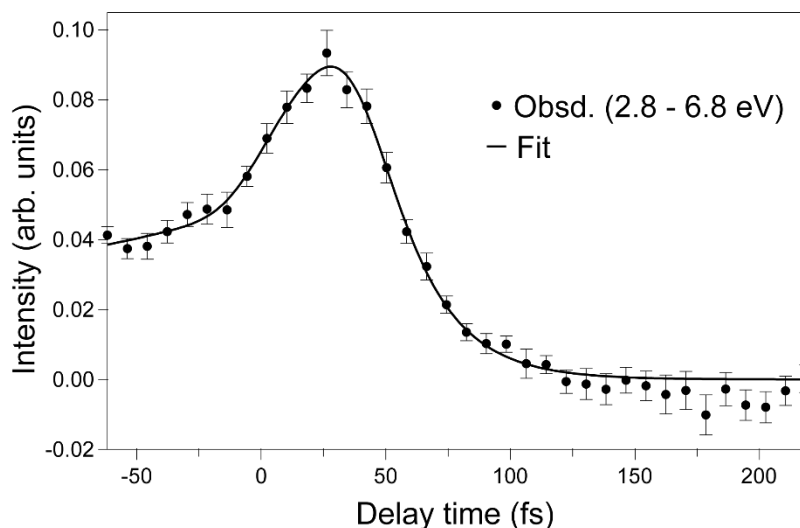
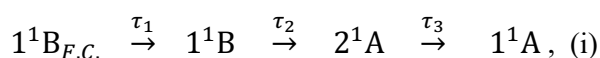


Figure S11 Photoelectron time profile (solid circles) obtained by 4.7/7.8-eV TRPEI. Photoelectron intensities were integrated over the eBE region of 2.8-6.8 eV in Fig. S10(b). The best-fit curve obtained by least-squares fitting using the kinetic model described in section S2 is shown as a solid line (see text).

S6. Comparison with other studies

So far, several experimental studies using TRPES, time-resolved mass spectrometry, and ultrafast soft X-ray absorption spectroscopy on the electronic dynamics of the ring-opening reaction of CHD have been performed, and the results are summarized in Table S6 along with those from the present study. A few common features in the previous experiments are as follows. (1) The bandwidths of the pump pulses were narrower than ours, so that the vibrational wave packet created in the 1^1B state was spatially broader and less localized. (2) The probe photon energies were often insufficient for inducing one-photon absorption of transient species, and resonance enhanced multiphoton ionization made their spectral assignment more difficult than for one-photon ionization.

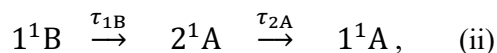
Fuß and coworkers performed ultrafast mass spectrometry using strong-field ionization with 800-nm (1.55-eV) probe pulses to observe time profiles of mass signals.²⁴ They proposed the following kinetic model,



where τ_1 represents the consumption time for a wave packet to leave the Franck-Condon (F.C.) region, and τ_2 and τ_3 are respectively the exponential decay time constants for $1^1B \rightarrow 2^1A$ and

$2^1A \rightarrow 1^1A$ internal conversion. The authors used an additional two time-constants to describe the dynamics of vibrationally hot CHD and HT molecules, which are not discussed here. Among these time constants, only the two time-constants τ_2 (43 ± 3 fs) and τ_3 (77 ± 7 fs) were ‘readable’ in their experimental data. Later, they performed the experiment with a superior time resolution of 13 fs to determine τ_1 , τ_2 and τ_3 to be 21, 35 and 80 fs, respectively.²⁵ Fuß and coworkers assumed a relatively long τ_2 , whereas other research groups did not consider this time constant as the wave packet passes through the CoIn region in the descending part of the potential energy surface.

Weber and coworkers performed a series of TRPES experiments on the ring-opening reaction of CHD. Kuthirummal et al. employed 267 nm pump and 400 nm probe pulses and observed the transient photoionization signal.²⁶ Resonance-enhanced two-photon ionization via Rydberg states was employed to observe the excited state dynamics. The photoionization signal appeared with a finite delay time. They postulated that the excited state responsible for the signal was 2^1A and employed the following kinetic model:



where τ_{1B} and τ_{2A} represent the exponential decay time constants for 1^1B and 2^1A , respectively. They reported these values to be 55 and 84 fs, respectively. Pemberton et al. observed a broad photoelectron signal rising with the time constant of 142 fs, which they assigned to photoionization of HT.²⁷ They reevaluated τ_{1B} to be 30 ± 2 fs.²⁷ It is noted, however, that ionization with a probe photon energy of 3.85 eV as employed by Pemberton et al. was possible only from the Franck-Condon region of the 1^1B state with an eBE of about 3.6 eV. The pump pulse bandwidth of 0.07 eV created a relatively narrow momentum distribution and a large spatial distribution, which was manifested by a vibrational progression resolved in their photoelectron spectra.

Table S6 Cross-correlation time, $\Delta t_{\text{C.C.}}$, dynamical time constants (fs) reported in previous experiments along with those obtained in this work.

Experiments ^a	Year	$\Delta t_{\text{C.C.}}$	Time constant ^b	Total ^c	Model ^d
Fuss et al. ²⁴	2000	~150	$\tau_1 = 10, \tau_2 = 43, \tau_3 = 77$	130	(i)
Kuthirummal et al. ²⁶	2006	~200	$\tau_{1B} = 55, \tau_{2A} = 84$	139	(ii)
Kosma et al. ²⁵	2009	13	$\tau_1 = 21, \tau_2 = 35, \tau_3 = 80$	136	(i')
Adachi et al. ²⁸	2015	80	$\tau_{1B} = 70 \pm 10, \tau_{2A} = 60 \pm 20$	130	(ii)
Pemberton et al. ²⁷	2015	100	$\tau_{1B} = 30 \pm 2^d$	–	–
Schalk et al. ²⁹	2016	125	$t_{\text{inc}} = 35 \pm 10^e, \tau = 60 \pm 10$	95	(iii)
Attar et al. ³⁰	2017	120	$\tau_{1B} = 60 \pm 20, \tau_{2A} = 110 \pm 600$	170	(ii)
This work 1 FWM ^f +HHG	2020	48	$t_{\text{ind}} = 32, \tau_{1B} = 0 \text{ and } 56, \tau_{2A} = 24$	56	(A)
This work 2 FFWM ^f	2020	31	$t_{\text{ind}} = 30 \pm 4, \tau_{1B} = 0, \tau_{2A} = 21 \pm 2$	51	(A)

^aIn all experiments, the pump photon energies are in 4.6 – 4.7 eV.

^bSee the text for the definition of respective time constants.

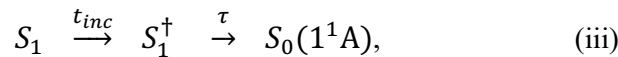
^cSum of all time-constants.

^dSee the text.

^eThis model employs a tri-exponential decay function for determination of $\tau_1, \tau_2,$ and τ_3 .

^fFilamentation four-wave mixing.

Schalk et al.²⁹ performed a similar TRPES experiment to that of Weber and coworkers, and their 2D photoelectron map was consistent with that of Pemberton et al. However, Schalk et al. employed a different kinetic model:



where t_{inc} is referred to as the “incubation time”, during which S_1 does not decay into S_0 (CHD or HT); notice that they assumed a single surface for S_1 . With model (iii), Schalk et al. estimated t_{inc} and τ to be 35 ± 10 and 60 ± 10 fs, respectively. These values were supported by their computational simulation, where t_{inc} and τ were calculated to be 29 and 52 fs, respectively.²⁹

Adachi et al. performed a 270-nm pump and 90-nm probe experiment.²⁸ They estimated the population in the 1^1B and 2^1A states from the photoelectron intensities for eBE values of 5.0 and 5.3 eV. Based on the results obtained in the present study, these eBE values were not best suited for monitoring the depopulations of these electronic states. As for formation of HT and hot CHD, their measurements were hampered by coherent artifacts for pump-probe delay times of less than 200 fs. They observed that the photoelectron signal from

CHD and bleach recovery gradually occurred after 200 fs, which contradicted other experimental studies. The cause of this discrepancy is unclear; however, since Adachi et al. needed to magnify the spectral intensity by 200 times to find the pump-probe signal, the low S/N ratio presumably hampered accurate measurements.

Computational studies on this benchmark system have been performed extensively, as summarized in Table S7. These studies calculated the time dependence of the population in different electronic states. As is typical for internal conversion mediated by CoIn, the excited state population does not decrease until the wave packet arrives at the CoIn region. The time prior to arrival of the wave packet (or classical trajectory) at the crossing region is termed the “latency time” in some of these studies. Tamura et al. estimated that the wave packet reaches CoIn with 2^1A in 15-25 fs. As seen in Table S7, most of these theoretical studies estimated t_{lat} to be 10-30 fs. On the other hand, a wide range of values from 47 to 234 fs have been reported for the $1/e$ decay time (τ) for the calculated S_1 population after t_{lat} . One thing to keep in mind is that theoretical calculations assume different bandwidths for the excitation pulses. The most recent simulations by Wolf et al. and Polyak et al. considered 0.3 and 0.26 eV, respectively, which are close to our experimental condition (~ 0.14 eV).

Wolf et al. found that the S_2 adiabatic state is never significantly populated, because the wave packet mostly propagates the avoided crossing region. Thus, they calculated the S_1 and S_0 populations and obtained t_{lat} and τ values of ~ 20 and 139 ± 25 fs, respectively. The latter value was obtained by single-exponential fitting to the calculated S_1 population including t_{lat} . Polyak et al. considered three states (S_2 , S_1 , and S_0) in their simulation and found that, while the majority of the S_1 population directly decays into S_0 , 10% is transferred to S_2 within 25 fs, and the up-funneled S_2 population decays within 200 fs. Since the time constants for S_0 population growth are complementary to those for the overall decay of the excited-state population, they proposed values of 16 ± 2 and 73 ± 9 fs, respectively, for t_{lat} and τ , which provides an overall reaction time of 89 ± 9 fs. As mentioned in section S2, while we also found that 12% of the S_1 population is transferred to S_2 , the majority of the S_1 population directly decays into S_0 , which qualitatively supports these theoretical simulations. Thus, in the present study, we propose an overall reaction time of 60 fs calculated as the sum of t_{ind} and τ_{2A} . Our experimental value is, however, significantly shorter than the values of 139 ± 25 or 89 ± 9 fs predicted by these theoretical simulations.

Table S7 Latency time, t_{lat} , and $1/e$ decay time constant, τ , (fs) for S_1 state reported based on theoretical simulations.

Simulations	Year	t_{lat}	τ	Total
Tamura et al. ³¹	2006	15 – 25 ^a	130 – 180 ^a	150 – 200
Ohta et al. ³²	2015	21	47	68
Lei et al. ³³	2016	~30	82	120 ^b
Schalk et al. ²⁹	2016	29	52	81
Attar et al. ³⁰	2017	30	–	106 ^c
Wolf et al. ³⁴	2019	~20	–	139 ± 25 ^b
Polyak et al. ³⁵	2019	16 ± 2 ^d	73 ± 9 ^d	89 ± 9 ^d
Filatov et al. ³⁶	2019	43 ± 5	234 ± 8	277

^aEstimated from trajectory analysis.

^bEstimated from a single-exponential fit to the calculated S_1 population including the latency time.

^cReported as “overall decay time constant”.

^dEstimated from the time constants of S_0 population growth, which are complementary to those of the overall excited states (S_2 and S_1) population decays (see the text).

S7. Semiempirical simulation of non-adiabatic dynamics and TRPES.

We simulated non-adiabatic dynamics following the UV photoexcitation of CHD using Tully’s fewest switches surface hopping with the semiempirical electronic structure method AM1 implemented in MOPAC.³⁷ Configuration interaction with single and double excitations in an active space of 6 electrons in 6 frontier orbitals was used to obtain the excited state energies and their gradients. Scalar non-adiabatic couplings were calculated as overlaps between adiabatic wavefunctions at subsequent time steps. The initial nuclear coordinates and velocities were sampled from a harmonic Wigner distribution for the geometry-optimized CHD. One thousand trajectories were launched on the bright $\pi\pi^*$ state and propagated for 1000 fs with a time step of 0.1 fs by allowing non-adiabatic transitions among the lowest four states. Dyson orbitals for ionization from the neutral electronic state to the lowest eight cationic states were computed at each time step. The electron binding energy, $e\text{BE}_{\text{fi}}(t)$, was obtained from the energy difference between the neutral and cationic state, and the intensity of each ionization channel ($D_{\text{f} \leftarrow S_i}$) was taken from the norm of the Dyson orbital $|\text{Dyson}_{\text{fi}}|$. Shown in Fig. S12a is the simulated TRPES obtained by combining the curves $(x(t), y(t)) = (t, e\text{BE}_{\text{fi}}(t))$ for all ionization channels with the weights $z(t) = |\text{Dyson}_{\text{fi}}|(t)$. We additionally performed simulation (not shown) with the trajectories starting in the ground state using FISH (field induced surface hopping).³⁸

An explicit electric field of Gaussian-shaped pulse (FWHM=48 fs) with a carrier frequency corresponding to the photon energy of 4.35 eV (resonant with the theoretical excitation energy of the 1^1B state) created a superposition of S_1 and S_2 . However, no qualitative difference was observed between the result and that obtained by excitation to a single 1^1B surface.

The simulated TRPES map clearly shows four bands at eBE=4, 6, 8 and 10 eV, while the simulation provided a longer reaction time and more complex S_1 - S_2 interactions than the experimental result (Fig. S12b). These point to limited accuracy of our calculations. However, the main objective of our simulation was to predict photoelectron spectra of vibrationally excited CHD and HT products, which are shown in Fig. 4(A) in the main text. For obtaining those spectra, the stick spectra of the two photoproducts were convolved with a Lorentzian of FWHM=0.5 eV. The average nuclear temperature at the final time step amounted to 1900 K. Meanwhile, Fig. 12a does not exhibit any oscillatory fluctuations of the bands at 8 and 10 eV. This is attributed to the limitation that surface hopping calculations neglect the quantum nature of the nuclei. We find that vibrational excitation, upon C_5 - C_6 bond rupture, of the torsional modes of the two $\text{C}=\text{C}$ arms dissipates rapidly into other vibrations in several hundred femtoseconds, which is similar to the dephasing time of the experimentally observed quantum beat. As seen in Fig. 12a, eBEs are affected by high-frequency modes (mostly $\text{C}-\text{C}$ stretch vibrations) but not by low-frequency modes. The simulation suggests that coherent excitation of 1^1B and 2^1A does not create a quantum beat in the reaction products, because the energy gap between the two states rapidly changes during the reaction.

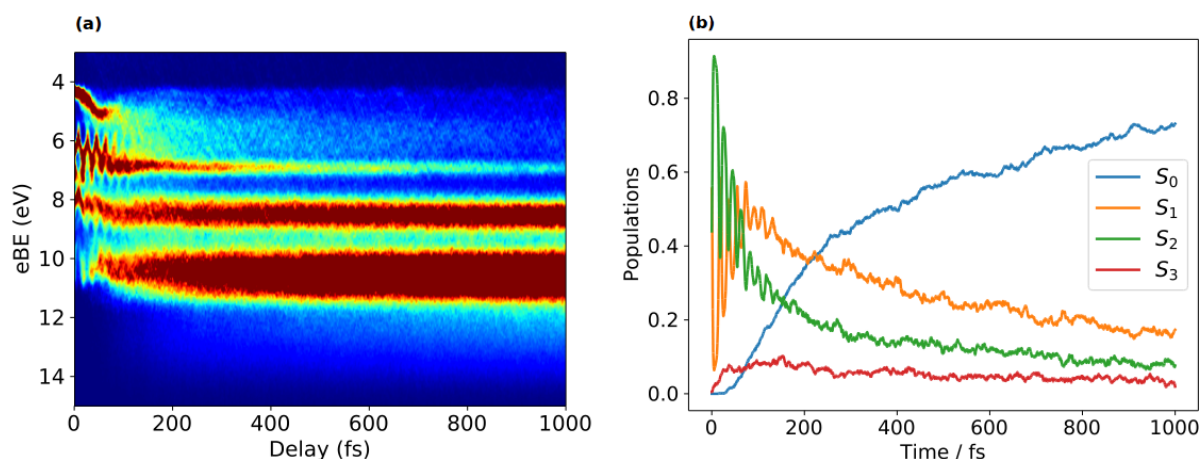


Figure S12 (a) Simulated time-resolved photoelectron spectrum. (b) Adiabatic state populations.

References

- 1 Nishitani, J., Yamamoto, Y., West, C. W., Karashima, S. & Suzuki, T., Binding energy of solvated electrons and retrieval of true UV photoelectron spectra of liquids, *Sci. Adv.* **5** (2019).
- 2 Fuji, T., Horio, T. & Suzuki, T., Generation of 12 fs deep-ultraviolet pulses by four-wave mixing through filamentation in neon gas, *Opt Lett* **32**, 2481-2483 (2007).
- 3 Corkum, P. B., Plasma perspective on strong-field multiphoton ionization, *Phys. Rev. Lett.* **71**, 1994-1997 (1993).
- 4 Lewenstein, M., Balcou, P., Ivanov, M. Y., L'huillier, A. & Corkum, P. B., Theory of high-harmonic generation by low-frequency laser fields, *Phys. Rev. A* **49**, 2117-2132 (1994).
- 5 Marceau, C., Hammond, T. J., Naumov, A. Y., Corkum, P. B. & Villeneuve, D. M., Wavelength scaling of high harmonic generation for 267 nm, 400 nm and 800 nm driving laser pulses, *J. Phys. Commun.* **1**, 015009 (2017).
- 6 Frassetto, F. *et al.*, Single-grating monochromator for extremeultraviolet ultrashort pulses, *Opt Lett* **19**, 19169-19181 (2011).
- 7 Kruit, P. & Read, F. H., Magnetic-field parallelizer for 2π electron-spectrometer and electron-image magnifier, *J. Phys. E: Sci. Instrum.* **16**, 313-324 (1983).
- 8 Widmark, P.-O., Malmqvist, P.-Å. & Roos, B. O., Density matrix averaged atomic natural orbital (ANO) basis sets for correlated molecular wave functions, *Theor. Chim. Acta* **77**, 291-306 (1990).
- 9 Werner, H.-J., Knowles, P. J., Knizia, G., Manby, F. R. & Schütz, M., Molpro: A general-purpose quantum chemistry program package, *WIREs Comput. Mol. Sci.* **2**, 242-253 (2012).
- 10 Werner, H.-J. *et al.*, *MOLPRO*, version 2012.1, Cardiff, U.K. (2012).
- 11 Werner, H. J. & Knowles, P. J., A second order multiconfiguration SCF procedure with optimum convergence, *J. Chem. Phys.* **82**, 5053-5063 (1985).
- 12 Knowles, P. J. & Werner, H.-J., An efficient second-order MC SCF method for long configuration expansion, *Chem. Phys. Lett.* **115**, 259-267 (1985).
- 13 Werner, H.-J., Third-order multireference perturbation theory The CASPT3 method, *Mol. Phys.* **89**, 645-661 (1996).
- 14 Shiozaki, T., Gyorffy, W., Celani, P. & Werner, H.-J., Communication: Extended multi-state complete active space second-order perturbation theory: energy and nuclear gradients, *J. Chem. Phys.* **135**, 081106 (2011).
- 15 Roos, B. O. & Andersson, K., Multiconfigurational perturbation theory with level shift the Cr_2 potential revisited, *Chem. Phys. Lett.* **245**, 215-223 (1995).

- 16 Honda, Y., Shida, T. & Nakatsuji, H., Excitation spectra of cation and anion radicals of several unsaturated hydrocarbons: Symmetry adapted cluster-configuration interaction theoretical study, *J. Phys. Chem. A* **116**, 11833-11845 (2012).
- 17 Kimura, K., Katsumata, S., Achiba, Y., Yamazaki, T. & Iwata, S., *Handbook of HeI photoelectron Spectra of Fundamental Organic Molecules* (Japan Scientific Societies, Tokyo, Japan, 1981).
- 18 Merchán, M. *et al.*, Electronic spectra of 1,4-cyclohexadiene and 1,3-cyclohexadiene: A combined experimental and theoretical investigation, *J. Phys. Chem. A* **103**, 5468-5476 (1999).
- 19 McDiarmid, R., Sabljic, A. & Doering, J. P., Valence transitions in 1,3-cyclopentadiene, 1,3-cyclohexadiene, and 1,3-cycloheptadiene, *J. Chem. Phys.* **83**, 2147-2152 (1985).
- 20 Horio, T., Spesyvtsev, R. & Suzuki, T., Simultaneous generation of sub-20 fs deep and vacuum ultraviolet pulses in a single filamentation cell and application to time-resolved photoelectron imaging, *Opt. Express* **21**, 22423-22428 (2013).
- 21 Even, U., Jortner, J., Noy, D., Lavie, N. & Cossart-Magos, C., Cooling of large molecules below 1 K and He clusters formation, *J. Chem. Phys.* **112**, 8068-8071 (2000).
- 22 Garcia, G. A., Nahon, L. & Powis, I., Two-dimensional charged particle image inversion using a polar basis function expansion, *Rev. Sci. Instrum.* **75**, 4989-4996 (2004).
- 23 Ruddock, J. M. *et al.*, A deep UV trigger for ground-state ring-opening dynamics of 1,3-cyclohexadiene, *Sci. Adv.* **5** (2019).
- 24 Fuß, W., Schmid, W. E. & Trushin, S. A., Time-resolved dissociative intense-laser field ionization for probing dynamics: Femtosecond photochemical ring opening of 1,3-cyclohexadiene, *J. Chem. Phys.* **112**, 8347-8362 (2000).
- 25 Kosma, K., Trushin, S. A., Fuß, W. & Schmid, W. E., Cyclohexadiene ring opening observed with 13 fs resolution: Coherent oscillations confirm the reaction path, *Phys.Chem.Chem.Phys.* **11**, 172-181 (2009).
- 26 Kuthirummal, N., Rudakov, F. M., Evans, C. L. & Weber, P. M., Spectroscopy and femtosecond dynamics of the ring opening reaction of 1,3-cyclohexadiene, *J. Chem. Phys.* **125**, 133307 (2006).
- 27 Pemberton, C. C., Zhang, Y., Saita, K., Kirrander, A. & Weber, P. M., From the (1B) spectroscopic state to the photochemical product of the ultrafast ring-opening of 1,3-cyclohexadiene: A spectral observation of the complete reaction path, *J. Phys. Chem. A* **119**, 8832-8845 (2015).
- 28 Adachi, S., Sato, M. & Suzuki, T., Direct observation of ground-state product formation in a 1,3-cyclohexadiene ring-opening reaction, *J. Phys. Chem. Lett.* **6**, 343-346 (2015).

- 29 Schalk, O. *et al.*, Cyclohexadiene revisited: A time-resolved photoelectron spectroscopy and ab initio study, *J. Phys. Chem. A* **120**, 2320-2329 (2016).
- 30 Attar, A. R. *et al.*, Femtosecond X-ray spectroscopy of an electrocyclic ring-opening reaction, *Science* **356**, 54-58 (2017).
- 31 Tamura, H., Nanbu, S., Ishida, T. & Nakamura, H., Ab initio nonadiabatic quantum dynamics of cyclohexadiene/hexatriene ultrafast photoisomerization, *J. Chem. Phys.* **124**, 084313 (2006).
- 32 Ohta, A., Kobayashi, O., Danielache, S. O. & Nanbu, S., Nonadiabatic ab initio molecular dynamics of photoisomerization reaction between 1,3-cyclohexadiene and 1,3,5-cis-hexatriene, *Chem. Phys.* **459**, 45-53 (2015).
- 33 Lei, Y. B., Wu, H. Y., Zheng, X. L., Zhai, G. H. & Zhu, C. Y., Photo-induced 1,3-cyclohexadiene ring opening reaction: Ab initio on-the-fly nonadiabatic molecular dynamics simulation, *J. Photoch. Photobio. A* **317**, 39-49 (2016).
- 34 Wolf, T. J. A. *et al.*, The photochemical ring-opening of 1,3-cyclohexadiene imaged by ultrafast electron diffraction, *Nat. Chem.* **11**, 504-509 (2019).
- 35 Polyak, I., Hutton, L., Crespo-Otero, R., Barbatt, M. & Knowles, P. J., Ultrafast photoinduced dynamics of 1,3-cyclohexadiene using XMS-CASPT2 surface hopping, *J. Chem. Phys.* **15**, 3929-3940 (2019).
- 36 Filatov, M., Min, S. K. & Kim, K. S., Non-adiabatic dynamics of ring opening in cyclohexa-1,3-diene described by an ensemble density-functional theory method, *Mol. Phys.* **117**, 1128-1141 (2019).
- 37 MOPAC2016, James J. P. Stewart, Stewart Computational Chemistry, Colorado Springs, CO, USA, [HTTP://OpenMOPAC.net](http://OpenMOPAC.net) (2016)
- 38 Mitrić, R., Petersen, J. & Bonačić-Koutecký, *Phys. Rev. A* **79**, 53416 (2009).